Degradation of Formaldehyde over MnO₂/CeO₂ Hollow Spheres: Elucidating the Influence of Carbon Sphere Self-Sacrificing Templates

Chen Zhu,[§] Shengnan Guan,[§] Wenzhi Li,* Ajibola T. Ogunbiyi, Kun Chen, and Qi Zhang*

Read Online

ACCESS | 📊 Metrics & More | 📖 Article Recommendations | 🔗 Supporting Information

ABSTRACT: Here, we prepare a MnO₂/CeO₂ hollow sphere catalyst using the carbon sphere as a self-sacrificing template for formaldehyde (HCHO) removal. In the feed gas of 20 ppm of HCHO (balanced by N₂) + 20 vol % O₂, a HCHO removal efficiency of 70% was achieved at 20 °C and full conversion was reached at around 47 °C at GHSV = 50,000 mL $(g_{cat} h)^{-1}$ for MnO₂/CeO₂ hollow spheres. The catalytic performance and structural and chemical properties of MnO₂/CeO₂ hollow spheres for the removal of core carbon spheres were explored, and the influence of using the carbon sphere as a self-sacrificing template was proved by comparing with carbon@MnO₂/CeO₂ (a core carbon sphere with a MnO₂/CeO₂ shell) and nonmorphologic MnO₂/CeO₂. The properties of the MnO₂/CeO₂ hollow spheres are significantly improved compared to carbon@MnO₂/CeO₂ (removal efficiency of 45% at 150 °C) and MnO₂/CeO₂ (removal efficiency of 46% at 20 °C) as a result of an evolution in the interaction between Mn/Ce and carbon. This increase in the interaction strength seems to (i) increase the oxygen vacancy, (ii) promote the oxygen species mobility, and (iii) improve the chemical stability of the MnO₂/CeO₂ hollow spheres. We believe that these results are beneficial to the fabrication of binary transition metal oxides and applications of them in HCHO removal.
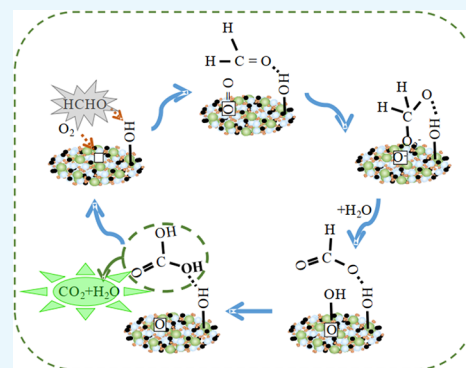
1. INTRODUCTION

As the most abundant carbonyl-containing VOCs in the atmosphere,[1] formaldehyde (HCHO) is a dominant indoor air pollutant released from furniture and decorating materials, building, and so on and can cause respiratory diseases, immune system disorders, and central nervous system damage.[2] Also, the excess rate of HCHO in Shanghai and Hangzhou respectively reached 24.2 and 38.9%.[3,4] Thus, the treatment of formaldehyde removal needs to be developed. In the past two decades, several categories of methods including physical adsorption, chemical adsorption, photocatalytic degradation, and thermal catalytic oxidation were proposed for the formaldehyde decontamination.[5−7] Among these methods, catalytic oxidation was regarded as a promising technology because it can completely oxidize gaseous formaldehyde into harmless H₂O and CO₂, only if a suitable catalyst is developed. The barriers of formaldehyde degradation technology are the difficulty in the design of cost-effective and highly active catalysts[8] and the enhancement of the synergistic effects of composite transition metal oxides.[9] Because the addition of noble-metal nanoparticles would hamper the practical application, Mn-, Co-, and Cu-based oxides[10,11] and their mixed oxides as non-precious-metal catalysts have been extensively studied. Among various transition metal oxides, Mn has been reported as one of the most active species for

HCHO removal because of its excellent redox property associated with the switch of Mn³⁺/Mn⁴⁺ states and varieties of crystal structures and morphologies.[12]

It is widely accepted that the interaction between mixed metal oxides makes their HCHO catalytic performance better than that of single metal oxides. Among them, the Mn/Ce binary oxides exhibit more superior activity than the other catalysts, which are one of the most promising "noble free" materials.[13] The catalytic performance of Mn/Ce oxide is related to its morphology. Therefore, we decided to study the morphology of the Mn/Ce oxide catalyst to explore the high-quality catalyst for HCHO removal.

Recently, a lot of efforts have been made to prepare hollow spherical metal oxides due to their superior properties over bulk materials as catalysts and fascinating structure features (e.g., tunable architecture and low density). For instance, Ma et al.[14] prepared Fe-Mn mixed oxide hollow microspheres using carbon spheres as sacrificial templates and used for
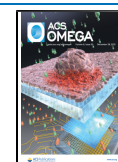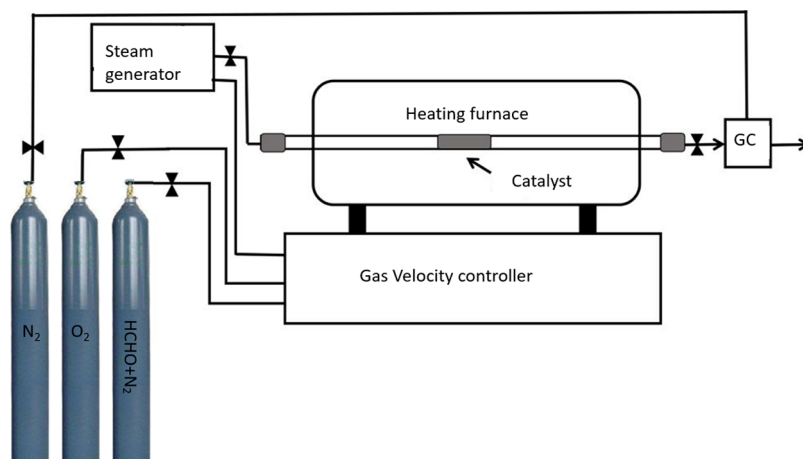
Scheme 1. Experimental Equipment Diagram

oxidation of 1,2-dichlorobenzene (DCB). The wonderful catalytic performance of $FeMnO_2$ is attributed to the combined effects of several factors, e.g., hierarchical porous structure and high surface active oxygen concentration. Meng et al.[15] prepared hollow MnO_x/CeO_2 oxides through the solvothermal method for catalytic oxidation of NO, which shows the NO conversion of 90.6% at 270 °C (GHSV = 120,000 mL $(g_{cat}$ h$)^{-1}$). It is believed that the hollow porous structure is beneficial. Zeng et al.[16] developed a solvothermal process followed by heat treatment for the preparation of murdochite-type Ni_6MnO_8 hollow spheres. The catalyst shows a remarkable long-term stability, which reduces 0.7% after 10 h of continuous testing. One of the factors leading to its excellent performance is its special morphologic structure.

Although the hollow structure could improve the performance of the catalysts, there have been a few studies in searching how the carbon sphere templates could affect the MnO_2/CeO_2 binary oxide and the mechanism for the enhanced formaldehyde removal performance. In this contribution, we investigated the effect of using carbon spheres as a sacrificial template for MnO_2/CeO_2 hollow spheres in formaldehyde removal. Through correlation between characterizations and catalytic performance, the electronic environment of MnO_2/CeO_2, reaction mechanism, and carbon sphere sacrificial template effect would be revealed. As will be discussed later, the sacrificial carbon sphere template played a very important role in expanding the size of adsorption sites, increasing the oxygen vacancy and improving the chemical stability of the MnO_2/CeO_2 hollow spheres. The effects of these variables on the HCHO removal were examined in detail with the MnO_2/CeO_2 hollow spheres, carbon@MnO_2/CeO_2 (a core carbon spheres with MnO_2/CeO_2 shell) nanospheres without air calcination to remove the carbon sphere template, and MnO_2/CeO_2 without carbon sphere templates. In addition, it was shown that HCHO can be effectively and permanently removed by the MnO_2/CeO_2 hollow spheres at low temperatures.

2. EXPERIMENTAL SECTION

2.1. Carbon Sphere Template Preparation. Typically, 70 mL of 0.5 M glucose aqueous (6.3 g) solution was placed in an 80 mL Teflon-sealed autoclave and kept at 180 °C (heating rate, 5 °C/min) for 5 h. After natural cooling, the black precipitates and puce suspension were isolated by centrifuga-

tion at a rate of 10,000 r/min and then washed with pure water. Several washing/centrifugation/redispersion cycles were conducted until the supernatant became transparent. The obtained products were calcined at 500 °C (heating rate, 5 °C/min) for 5 h in an Ar atmosphere.[17]

2.2. MnO_2/CeO_2 Hollow Sphere Preparation. First, 0.24 g of C nanospheres was dispersed in 80 mL of $KMnO_4$ (10 mM) aqueous solution. $Ce(NO_3)_3 \cdot 6H_2O$ (0.18 g) was added at the same time under ultrasonication for 1 h. Then, the suspension liquid was added into a Teflon-sealed autoclave and kept at 180 °C for 60 min. Then, the autoclave was picked up and cooled down to room temperature. Finally, the products were centrifuged at a rate of 10,000 r/min, then cleaned by three washing/centrifugation/redispersion cycles in water, and dried at 180 °C for 5 h in air. Carbon@MnO_2/CeO_2 was obtained by calcining the precursor in N_2 at 450 °C (heating rate, 5 °C/min) for 2 h. The MnO_2/CeO_2 hollow spheres were obtained by calcining the as-prepared carbon@MnO_2/CeO_2 in air at 450 °C (heating rate, 5 °C/min) for 2 h to remove the carbon core.

2.3. MnO_2/CeO_2 without the Carbon Nanosphere Preparation. The reference catalyst, MnO_2/CeO_2, was prepared using the same procedure as for the MnO_2/CeO_2 hollow spheres, except that no carbon spheres were added.

2.4. Characterization. X-ray diffraction was carried out on a Smartlab type XRD-meter (Japan) utilizing the Cu Kα radiation source with 40 kV tube voltage, 40 mA tube current, and 0.05° min^{-1} scanning speed. The SEM analysis was carried out on an XL-30ESEM apparatus (FEI Electronics Optics Corporation) at 30 and 5.0 kV voltages. The sample was prepared by ultrasonication in ethanol for 5 min and then placed on a carbon film. The 2θ of wide-angle XRD ranged from 20° to 80°. The N_2 desorption/adsorption experiment was carried out on an Autosorb-Tristar II 3020 M apparatus (Micromeritics Inc.). The sample was degassed at 300 °C for 4 h before measurement under vacuum. The N_2 desorption/adsorption isotherm was tested using the BJH method. The TEM image was obtained on a JEM-2100F apparatus (JEOL) at 200 kV voltage. The sample was also dispersed by ultrasonication in ethanol for 5 min and then put on the copper grid.

The Fourier-transform infrared spectra were carried out on a Nicolet 8700 FTIR spectrometer (American Thermo Nicolet Instrument Co.) at a resolution of 4 cm^{-1} in the range of 400–4000 cm^{-1}. Inductively coupled plasma atomic emission
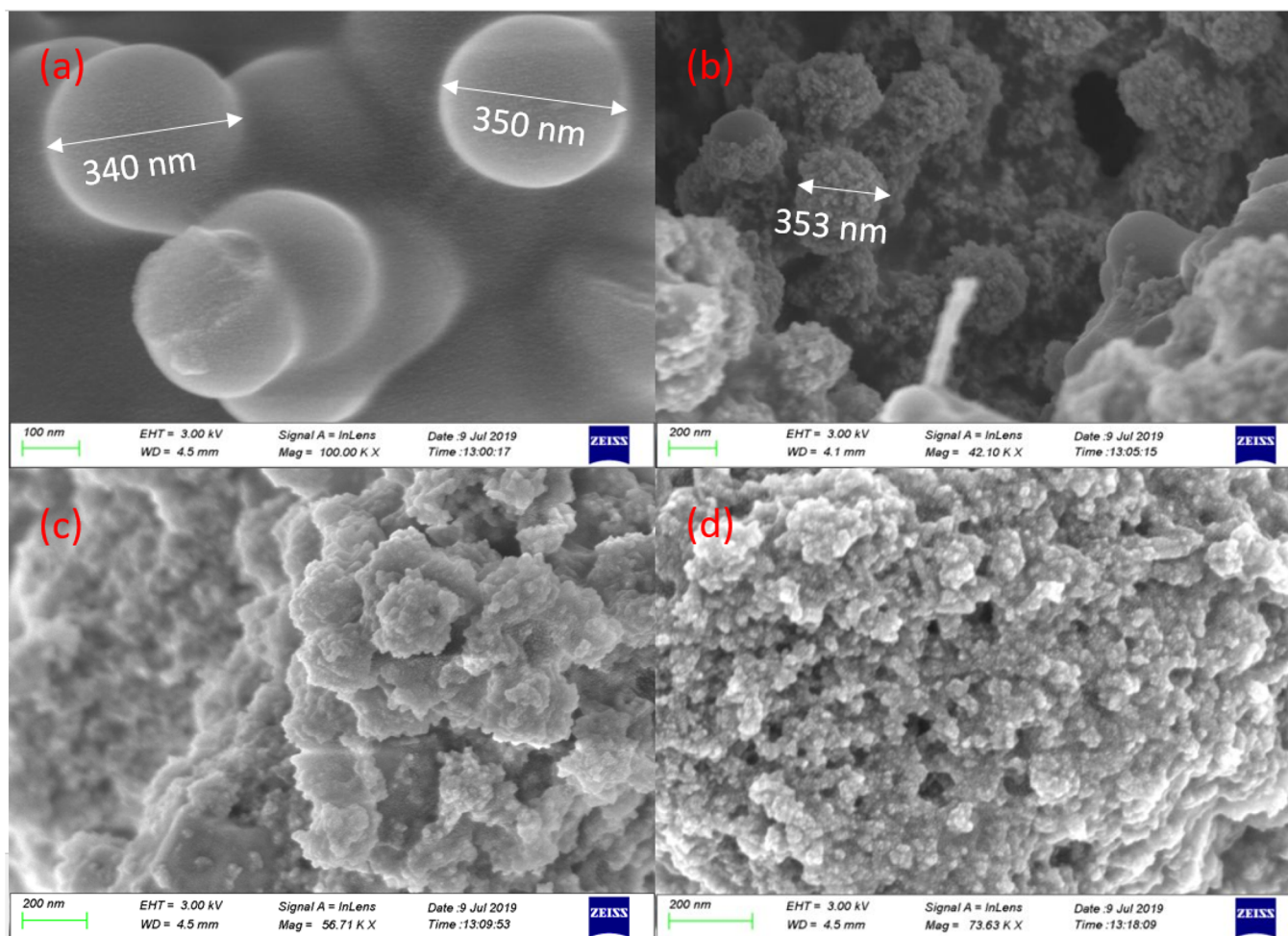
Figure 1. SEM patterns of (a) carbon nanospheres, (b) carbon@MnO$_2$/CeO$_2$, (c) MnO$_2$/CeO$_2$ hollow spheres, and (d) MnO$_2$/CeO$_2$ samples.

spectrometry (ICP-AES) was performed on an Optima 7300 DV instrument (PerkinElmer). In this work, temperature-programmed measurement includes temperature-programmed oxidation (TPO) and temperature-programmed reduction (TPR) experiments. The H$_2$-TPR was measured on a Quantachrome 1900 instrument. The samples were placed in a U tube and pretreated in a N$_2$ flow at 300 °C for 1 h. Then, the sample was cooled and reduced using a range of 30−900 °C at 10 °C/min in a 10% H$_2$−90% argon flow (50 mL/min). The H$_2$ consumption was calibrated by CuO (99.998%) and calculated by the integrated TPR peak areas. TPO was also carried out on this instrument. The sample was pretreated in a helium flow at 300 °C and oxidized in a 4% O$_2$/He flow in the range of 50−700 °C with a rate of 10 °C/min. The Raman spectra were measured on a LabRam-HR spectrometer (JY, France). XPS was carried out on an ESCALAB 250 (Thermo-VG Scientific) operating at 300 W, with an Mg Kα X-ray source. The C 1s at 284.6 eV was used to correct the effect of electric charge as the reference. The ratio of elements with different chemical valencies was computed using XPS-PEAK software through the peak area. In situ DRIFTS was performed on a Thermo Nicolet iS50 FTIR spectrometer in the 1100−4000 cm^{-1} range.

2.5. HCHO Oxidation. The catalytic activity was carried out by a fixed bed flow reactor at atmospheric pressure. The catalyst (60 mg) was loaded into a quartz tube and then put into a tube furnace (Scheme 1). Formaldehyde (20 ppm,

balanced by N$_2$) and 20 vol % O$_2$ were passed through the reaction bed at a flow rate of 50−120 mL/min (relative humidity, ~50%). The concentration of formaldehyde in the outlet gas was measured online by an online Kexiao 1690 gas chromatograph with the PQ column (AT.SE-30 (30 mm × 0.32 mm × 1.00 U)) and an flame ionization detector (FID) (set at 150 °C). The low-noise air pump model is MJK-2LB, and the hydrogen generator model is SGH-300A. The gas valve and an injection-volume loop (5 mL) were used to inject. The relative concentration of HCHO was obtained by integrating the formaldehyde peak. All reaction data were repeated three times to reduce errors. The formaldehyde conversion was calculated as follows:

$$\text{HCHO conversion(\%)} = \frac{[\text{HCHO}]_{in} - [\text{HCHO}]_{out}}{[\text{HCHO}]_{in}} \times 100\% \tag{1}$$

where $[\text{HCHO}]_{in}$ is the formaldehyde initial concentration in the feed gas, and $[\text{HCHO}]_{out}$ is the formaldehyde concentration after the reaction. For comparison, the catalytic performances of carbon@MnO$_2$/CeO$_2$ and MnO$_2$/CeO$_2$ were also measured.

3. RESULTS AND DISCUSSION

**3.1. SEM and TEM Characterization.** The SEM images of the samples are shown in Figure 1, which are used to
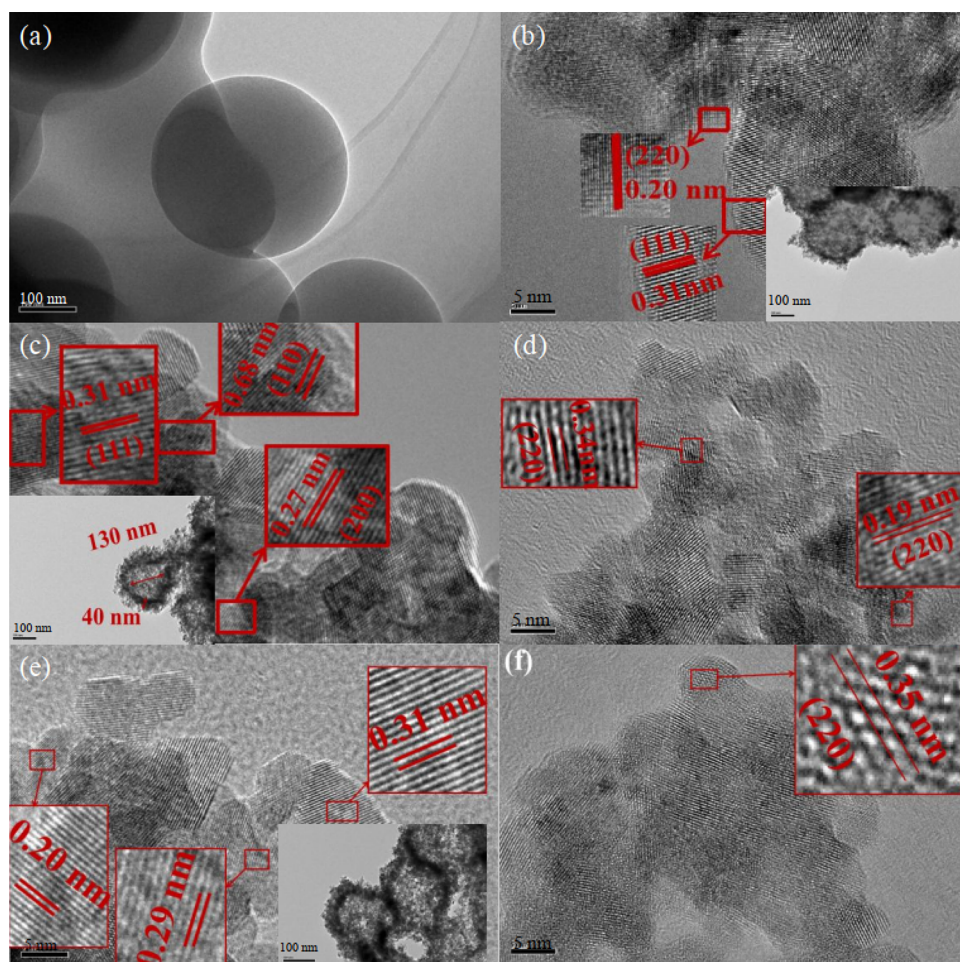
Figure 2. High-resolution TEM of (a) carbon nanospheres, (b) carbon@MnO_2/CeO_2, (c) MnO_2/CeO_2 hollow spheres, (d) used MnO_2/CeO_2 hollow spheres, (e) MnO_2/CeO_2, and (f) used MnO_2/CeO_2 samples.

compare the geometric structure differences between the catalysts. According to the mapping (Figure S1), we got carbon balls and loaded Mn and Ce on top of the carbon balls of carbon@MnO_2/CeO_2. However, if the precursor was calcined at 500 °C in the air, the carbon content decreased dramatically, but the overall structure remained spherical, which proved that the core of the original carbon ball was removed during the air calcination process, leaving behind Mn and Ce metal hollow spheres. The bare carbon spheres with smooth surfaces have a size range from 300 to 350 nm. MnO_2/CeO_2 hollow sphere and MnO_2/CeO_2 samples exhibit a rather different morphology. The coated spheres and MnO_2/CeO_2 hollow spheres exhibit a uniform spherical shape in Figure 1b,c, and the mean hollow spheres sizes are ~350 and ~210 nm, respectively. As for MnO_2/CeO_2, it has an amorphous morphology. The EDX mapping results reveal that in MnO_2/CeO_2 hollow spheres, Mn/Ce and C species are homogeneously dispersed. Also, it is proved that some residual carbon exists after calcination.

In addition, high-resolution TEM of catalysts is presented in Figure 2 and MnO_2/CeO_2 hollow spheres exhibit some floccule-like particles growing on external and internal surfaces, and they are loosely connected. As shown in the embedded diagram in Figure 2c, the internal diameter is about 130 nm and the shell thickness is about 40 nm for MnO_2/CeO_2 hollow spheres. Also, the internal diameter is about 130 nm and the shell thickness is about 40 nm (Figure S2). The spacings of the lattice fringe exhibited in HRTEM images are about 0.31, 0.27,

and 0.19 nm, which are attributed to the (111), (200), and (220) facets of CeO_2, respectively. Also, the adjacent fringe spacing of α-MnO_2 is ~0.68 nm, corresponding to the (110) diffraction plane. The next step is to explore how the sacrificial carbon sphere template will affect the performance of MnO_2/CeO_2 hollow spheres.

3.2. HCHO Removal Performance. Figure 3 illustrates the temperature dependence of the HCHO conversion at GHSV = 50,000 mL $(g_{cat} h)^{-1}$. In MnO_2/CeO_2 hollow spheres, the conversion of HCHO reaches 70% at 20 °C and reaches full conversion at around 47 °C, which is much lower than its performance of Ag/CeO_2 at 60 °C for $T_{100\%}$,[18] $Ni_{0.8}Co_{2.2}O_4$ at 60 °C for $T_{100\%}$,[19] and Au/CeO_2 at 60 °C for $T_{100\%}$.[20] As for MnO_2/CeO_2, the conversion of HCHO is 46% at 20 °C, which is much lower than that of MnO_2/CeO_2 hollow spheres, and reaches full conversion at around 50 °C. To determine the active sites in the sample, the removal of formaldehyde was conducted over carbon@MnO_2/CeO_2. For 20 ppm of formaldehyde, 45% removal efficiency was achieved at 150 °C with 20% O_2 at GHSV = 50,000 mL $(g_{cat} h)^{-1}$, indicating that the active sites for the reaction are mainly on manganese/cerium oxide. Since the activities of the MnO_2/CeO_2 hollow spheres are better than those of MnO_2/CeO_2 at low temperatures, we speculate that the electronic structure of Mn/Ce has been changed by the carbon sphere template after calcination and removal in the MnO_2/CeO_2 hollow spheres. The higher reaction rates need the facile adsorption of reaction
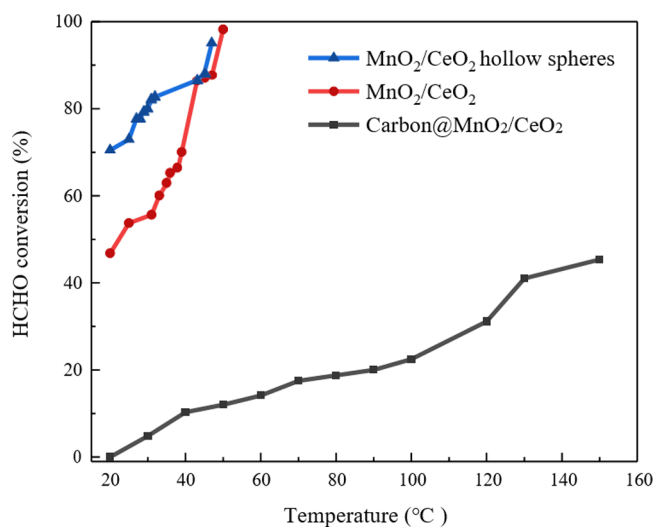
Figure 3. HCHO removal efficiencies (GHSV = 50,000 mL $(g_{cat} h)^{-1}$, RH = 50%) over the MnO_2/CeO_2 hollow spheres, MnO_2/CeO_2, and carbon@MnO_2/CeO_2 samples.

gases and intermediates, which requires catalysts with rich reaction sites. Thus, how does the sacrificial carbon sphere template improve the MnO_2/CeO_2 hollow spheres?

3.3. Phase Structures. To obtain detailed information on the phase structures of different catalysts, we characterized the samples using XRD, FTIR, TG−DTG, and Raman spectroscopy. As displayed in Figure 4, for the carbon nanospheres, the
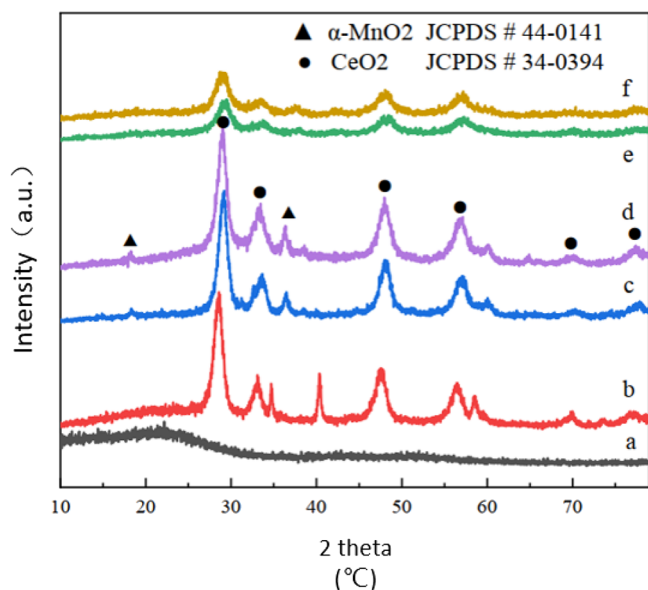
Figure 4. XRD patterns of (a) carbon nanospheres, (b) carbon@MnO_2/CeO_2, (c) MnO_2/CeO_2 hollow spheres, (d) used MnO_2/CeO_2 hollow spheres, (e) MnO_2/CeO_2, and (f) used MnO_2/CeO_2 samples.

XRD pattern shows the weak and broad peaks at about 23°, which are ascribed to the (002) planes of graphite. Also, the peaks at 76.90°, 69.67°, 59.38°, 56.56°, 47.73°, 33.27°, and 28.85° represent a typical cubic fluoride CeO_2 crystal phase (JCPDS 34-0394). The peaks at 18.36° and 36.38° correspond to (200) and (211) crystal planes of the body-centered tetragonal α-MnO_2 (JCPDS 44-0141).[21] After undergoing a

stability measurement at 60 °C for 72 h, the phase of the catalysts shows no obvious change for MnO_2/CeO_2 hollow spheres and MnO_2/CeO_2. The crystallite size of MnO_2/CeO_2 hollow spheres is slightly increased (10.40 → 10.49 nm) after the continuity test (Table 1). However, MnO_2/CeO_2 with a

Table 1. Structural Parameters of the Catalysts

	crystallite size[a] (nm)	surface area (m² g⁻¹)	pore volume (×10⁻² cm³ g⁻¹)	pore size[b] (nm)	defect[c] (I_D/I_{F2g})
carbon nanosphere		230.7	16	2.2	
carbon@ $MnO_2/$ CeO_2	10.6	186.3	21	3.6	
MnO_2/CeO_2 hollow spheres	10.4	44.1	20	17.1	48%
used $MnO_2/$ CeO_2 hollow spheres	10.0	46.0	20	16.4	49%
MnO_2/CeO_2	10.5	118.6	45	13.7	43%
used $MnO_2/$ CeO_2	9.8	111.9	44	13.6	46%

[a]Calculated by the Scherrer equation ($D = K\lambda/(\beta \cos \theta)$). [b]Calculated by the BJH method. [c]Calculated from the Raman spectra.

mean crystallite size of 10.02 nm is slightly decreased to 9.76 nm after the continuity test, which could be attributed to the aggregation of the MnO_2/CeO_2 nanoparticles.

Meanwhile, the functional group spectra collected on samples are compared through FTIR in Figure S3. The absorption peak at ∼572 cm⁻¹ is characteristic of Mn−O stretching vibration for MnO_2/CeO_2. The bands at 516 and 612 cm⁻¹ for MnO_2/CeO_2 hollow spheres correspond to Mn−C and Mn−O−Ce vibrations, while they are not observed for MnO_2/CeO_2. Also, the existence of C indicated the accelerated charge transport efficiency and the change in the electronic states of interacting Mn/Ce atoms. In addition, the peak at 1091 cm⁻¹ corresponds to the CeO_2 vibration. The peak at 1384 cm⁻¹ was attributed to bending vibrations of O−H groups combined with metal atoms, which would convert adsorbed HCHO into dioxymethylene species, while it is not observed for pristine MnO_2/CeO_2. The resonance at ∼1620 cm⁻¹ is assigned to the skeletal vibrations of unoxidized graphitic (C−C/C=C) domains for the carbon sphere. Its density decreases in carbon@MnO_2/CeO_2, implying that the C−C/C=C bond is broken and may form a C=O bond. Also, the band at 1635 cm⁻¹ and strong broadband at 3439 cm⁻¹ are attributed to the ν(OH) stretching vibration of intercalated water and adsorbed H_2O molecules on the sample surface. After the continuity test, groups such as −COOH, −CHO, and −OH were adsorbed on the catalyst surface, and the interatomic interaction changed the electron distribution, thus enhancing the IR absorption intensity, which is more intense on MnO_2/CeO_2 hollow spheres.

3.4. Textural Properties. To demonstrate the thermal stability of the catalysts, thermogravimetry and differential thermogravimetry (TG−DTG) analyses have been carried out in a nitrogen atmosphere, and results are compared in Figure 5. The MnO_2/CeO_2 hollow spheres and MnO_2/CeO_2 samples show 1.43 and 3.7% weight losses below 323 and 302 °C, respectively, which are assigned to the loss of chemical oxygen. However, there are 1.55 and 3.81% mass losses of the used
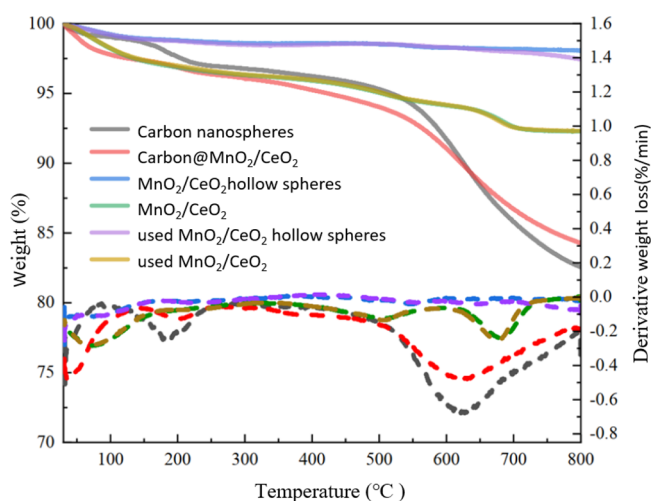
Figure 5. TG−DTG of different samples.

MnO_2/CeO_2 hollow spheres and MnO_2/CeO_2 samples below 323 and 350 °C, respectively, which are attributed to the decomposition of the product, in addition to the loss of chemical oxygen. For MnO_2/CeO_2, at around 300−597 °C, a weight loss of 2.14% is attributed to the loss of oxygen from MnO_2 and then transformation to Mn_2O_3. Another weight loss of 1.88% is attributed to the continuous loss of oxygen (phase transformation from Mn_2O_3 to Mn_3O_4) at 597−800 °C. Meanwhile, there is only phase transformation of MnO_2 to Mn_2O_3 (0.52% continuous weight loss) occurring in MnO_2/CeO_2 hollow spheres before 800 °C due to the strong bond force between C and Mn/Ce, which can effectively bind up the motion of C, Mn, and Ce and inhibits the aggregation and sintering of MnO_2/CeO_2 hollow spheres, leading to the higher stability. Moreover, it can be seen that this is a continuous weight loss, which confirmed that most of MnO_2 was probably amorphous instead of being crystalline. In addition, compared with pristine MnO_2/CeO_2, the temperatures of MnO_2-to-Mn_2O_3 and Mn_2O_3-to-Mn_3O_4 phase transformation for the used MnO_2/CeO_2 decrease by 30.5 and 8.3 °C, respectively. Meanwhile, the temperature with the used MnO_2/CeO_2 hollow spheres does not change, which indicates that MnO_2/CeO_2 hollow spheres are a more stable catalyst compared with MnO_2/CeO_2. However, at a temperature above 700 °C, the weight loss of the used MnO_2/CeO_2 hollow sphere sample is 0.58% higher than that of pristine MnO_2/CeO_2 hollow spheres, which means that the manganese/cerium interaction is reduced and little manganese cerium oxides are probably separated.

Figure S4 exhibits the N_2 adsorption−desorption curves and pore sizes of the samples, and Table 1 shows the S_{BET} and pore volume. The curves of MnO_2/CeO_2 hollow sphere gradual increase in the absorbed volume at a medium relative pressure $(0.4 < P/P_0 < 1.0)$ imply the presence of mesopores, while the curves of MnO_2/CeO_2 and carbon@MnO_2/CeO_2 increase in adsorbed volume at a high pressure and relatively low pressure indicate the presence of macropores (>50 nm) and micropores (<2 nm), respectively. The S_{BET} of the samples calculated from the nitrogen desorption data exhibits that the S_{BET} of MnO_2/CeO_2 is 118.6 m^2 g^{-1}, which is higher than that of the MnO_2/CeO_2 hollow spheres (44.08 m^2 g^{-1}). Meanwhile, the latter one performs better activity especially at a low temperature stage (<40 °C). The pore size distribution of the carbon

spheres showed unimodal porosity with an average of 2.203 nm. Also, the pore diameter of MnO_2/CeO_2 hollow spheres is about 17.11 nm due to slit-like mesopores resulting from MnO_2/CeO_2 nanosheets and consistent with the SEM results. Thus, it can be seen that there is no clear correlation between S_{BET}/pore size and performance in our test. In addition, the S_{BET} of MnO_2/CeO_2 sample decreases after the continuity test, while that of MnO_2/CeO_2 hollow spheres is not, which is due to the better chemical stability of MnO_2/CeO_2 hollow spheres compared to MnO_2/CeO_2, consistent with the TG−DTG results.

The presence of a higher amount of oxygen vacancies on MnO_2/CeO_2 hollow spheres was confirmed by Raman spectroscopy. Figure 6 indicates that the concentration of
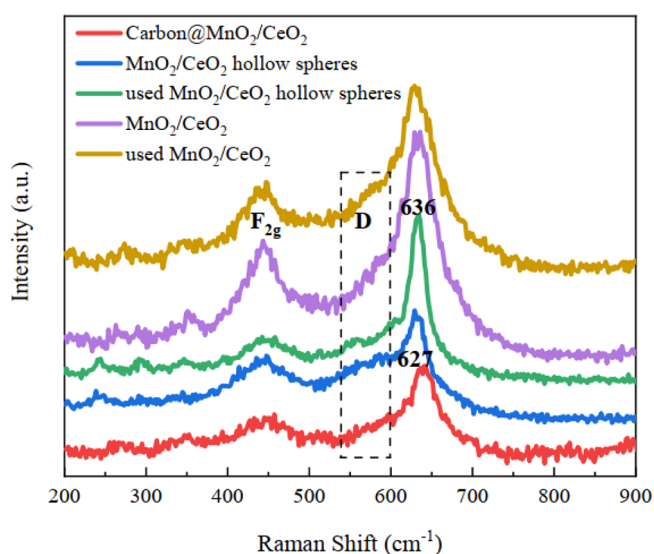

Figure 6. Raman spectra of the catalysts.

surface oxygen vacancies in MnO_2/CeO_2 hollow spheres (48%) is higher than that in MnO_2/CeO_2 (43%), as calculated by the defect-related peak intensity ratio at 585 cm^{-1} to F_{2g} at 444 cm^{-1} (I_D/I_{F2g}) shown in Table 1.[22,23] The MnO_2/CeO_2 hollow spheres have more defects, which could be explained by the strong interaction between MnO_2 and CeO_2 corroborated with FTIR results. Also, more surface oxygen vacancies would expose more undercoordinated Mn/Ce atoms to adsorb oxygen and provide delocalized electrons to surface-chemisorbed O_2. This would maintain a surface electrostatic balance and form more O_{ads} in the reaction. This is also corroborated by XPS analysis discussed below. The $\nu_{2(Mn-O)}$ of MnO_2/CeO_2 at 636 cm^{-1} shifts to 627 cm^{-1} for MnO_2/CeO_2 hollow spheres, and the peak shifts toward lower binding energies, implying the weaker interaction between O and Mn atoms. The presence of oxygen vacancies increases the electron density of O_{lat}; therefore, the binding energy decreases. For MnO_2/CeO_2 hollow spheres, the Mn−O bonds force weakening, therefore improving the O_{lat} reactivity and finally leading to higher formaldehyde conversion, which is consistent with the activities observed in Figure 3.

Moreover, the existence of more oxygen vacancies in MnO_2/CeO_2 hollow spheres would also be characterized by electron paramagnetic resonance (EPR) herein. As shown in Figure S5, the MnO_2/CeO_2 hollow spheres and MnO_2/CeO_2 exhibit obvious ESR signals at g = ~2.001, which corresponds with the
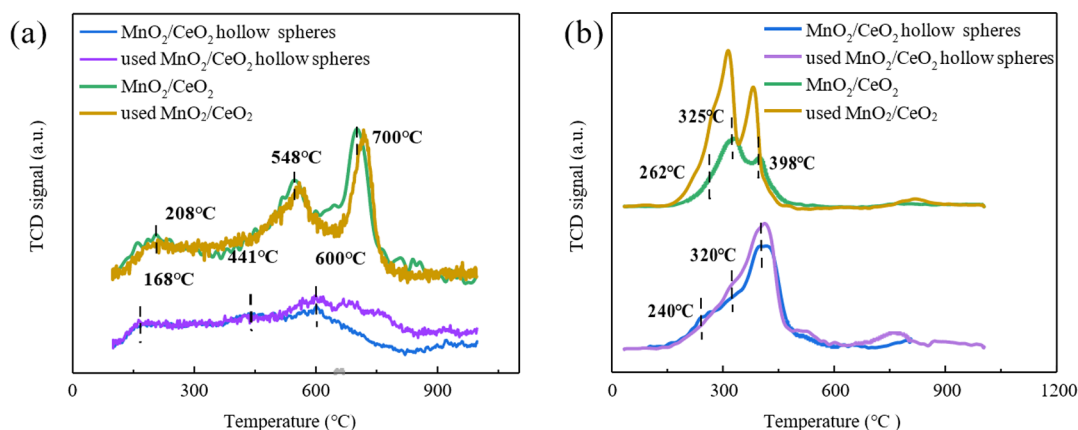
Figure 7. (a) O_2-TPD and (b) H_2-TPR of different samples.

typical signal of oxygen vacancies. Compared with the pristine samples, the ESR signal peak of the used MnO_2/CeO_2 hollow spheres possesses higher intensity, implying that the continuity test brings more defects into MnO_2/CeO_2 hollow spheres. The oxygen vacancy built the defect state, enabling more electrons to transfer from the valance band to the conduction band, bringing more active radical species. However, such an ESR signal cannot be found in the used MnO_2/CeO_2.

3.5. H_2-TPR and O_2-TPD Measurements. The nature of oxygen species in MnO_2/CeO_2 hollow spheres can also be inferred from O_2 temperature-programmed desorption (O_2-TPD) and H_2 temperature-programmed reduction (H_2-TPR) profiles.

As displayed in the O_2-TPD (Figure 7a), for MnO_2/CeO_2 hollow spheres, the peak at about 168 °C corresponds to the desorption of physical absorbed oxygen. Also, peaks at ~600 and 441 °C correspond to the desorption of lattice oxygen and the chemisorbed oxygen species, respectively. Compared to MnO_2/CeO_2, the MnO_2/CeO_2 hollow spheres exhibit a lower desorption temperature for the oxygen species, implying the higher mobility and reactivity of surface-active oxygen.

The H_2-TPR experiment result is shown in Figure 7b. The two intensity peaks at around 320 and 240 °C are attributed to the reduction of bulk oxygen and surface oxygen of MnO_2, respectively. Also, overlapping peaks appeared at a high temperature range of 397−427 °C, which is attributed to the reduction of different valence states of Mn/Ce mixed oxides. Compared with MnO_2/CeO_2, MnO_2/CeO_2 hollow spheres have a higher ratio of oxygen reduced at a high reduction temperature (~400 °C). It means that MnO_2/CeO_2 hollow spheres need a higher temperature to reduce, implying a strong interaction between Mn/Ce metal oxides. The strengthened interaction could be considered to improve the sintering resistance, while this would also lead to difficulty in reduction.

H_2-TPR results of the pristine samples and used samples are also compared as displayed in Figure 7b. It is observed that the reduction peak of the used MnO_2/CeO_2 hollow spheres located higher than that of the pristine samples. This suggests a stronger Mn/Ce metal oxide interaction. Meanwhile, for the used MnO_2/CeO_2, the reduction peaks locate lower than that of the pristine samples, meaning that some MnO_2 and CeO_2 species were segregated after the continuity test.

The above results indicate that MnO_2/CeO_2 hollow spheres can provide more mobile and active surface oxygen species to participate in the catalytic reaction than MnO_2/CeO_2 and have

a stronger Mn/Ce metal oxide interaction, leading to a better catalytic activity for formaldehyde oxidation.

For the Mn 2p XPS spectrum (Figure 8A), before the catalytic process, three peaks at ~640.5, ~641.7, and ~643.1 eV are ascribed to Mn(II), Mn(III), and Mn(IV) in the MnO_2/CeO_2 hollow spheres, and their relative contributions were increased by −4.65, 0.19, and 4.46%, respectively, after the continuity test. The results indicate that the valence state transformation of Mn(II)/Mn(III) and Mn(III)/Mn(IV) occurred on the surface of MnO_2/CeO_2 hollow spheres during the process of HCHO removal. For MnO_2/CeO_2, the relative contributions of Mn(II), Mn(III), and Mn(IV) to the overall Mn intensity changed from 22.38, 50.03, and 27.59% to 21.93, 51.38, and 26.68%, respectively, after the 72 h catalytic reaction. Furthermore, compared to MnO_2/CeO_2, the binding energy of Mn $2p_{3/2}$ peaks shifted to lower values for MnO_2/CeO_2 hollow spheres. The downshift was caused by an increase in the π electron cloud density after the indraught of carbon spheres, suggesting the presence of interfacial charge transfer from C to Mn atoms. It could be calculated that the ratio of Mn(IV) for MnO_2/CeO_2 hollow spheres (15.46%) is smaller than that for MnO_2/CeO_2 (27.59%), implying the higher ratio of Mn(II) and Mn(III) for MnO_2/CeO_2 hollow spheres, which is also related to the formation of oxygen vacancies to maintain charge balance, corroborated with Raman results. The Mn 3s core level spectra of catalysts are shown in Figure 8B, which indicated that the average oxidation states (AOS) of manganese ions[24] coincided with the ratio of Mn^{2+}, Mn^{3+}, and Mn^{4+} from Mn 2p, as shown in Table 2.

As shown in Table 2, the MnO_2/CeO_2 hollow spheres represent the higher ratio of Ce^{4+}/Ce (85.82%) than that for MnO_2/CeO_2 (78.59%), which is due to the stronger interaction between Mn and Ce to maintain electrostatic equilibrium. Remarkably, the strong oxygen storage ability of Ce^{4+} could replenish the surface-chemisorbed oxygen. The replenished O could regenerate surface oxygen, which improved the HCHO oxidation activity, and the large oxygen release and storage ability of Ce^{4+} enabled the conversion of Ce^{3+} to Ce^{4+}. Compared to MnO_2/CeO_2, the MnO_2/CeO_2 hollow sphere Mn $2p_{3/2}$ peak shifts to the lower binding energy due to the oxidizing effect by C and the electrons transferring from Ce; accordingly, the MnO_2/CeO_2 hollow sphere Ce 3d peak shifts to the higher binding energy (Figure 8C), attributed to the electrons transferring to Mn/O. The electron transfer between manganese and cerium also indicates that their interaction is stronger.
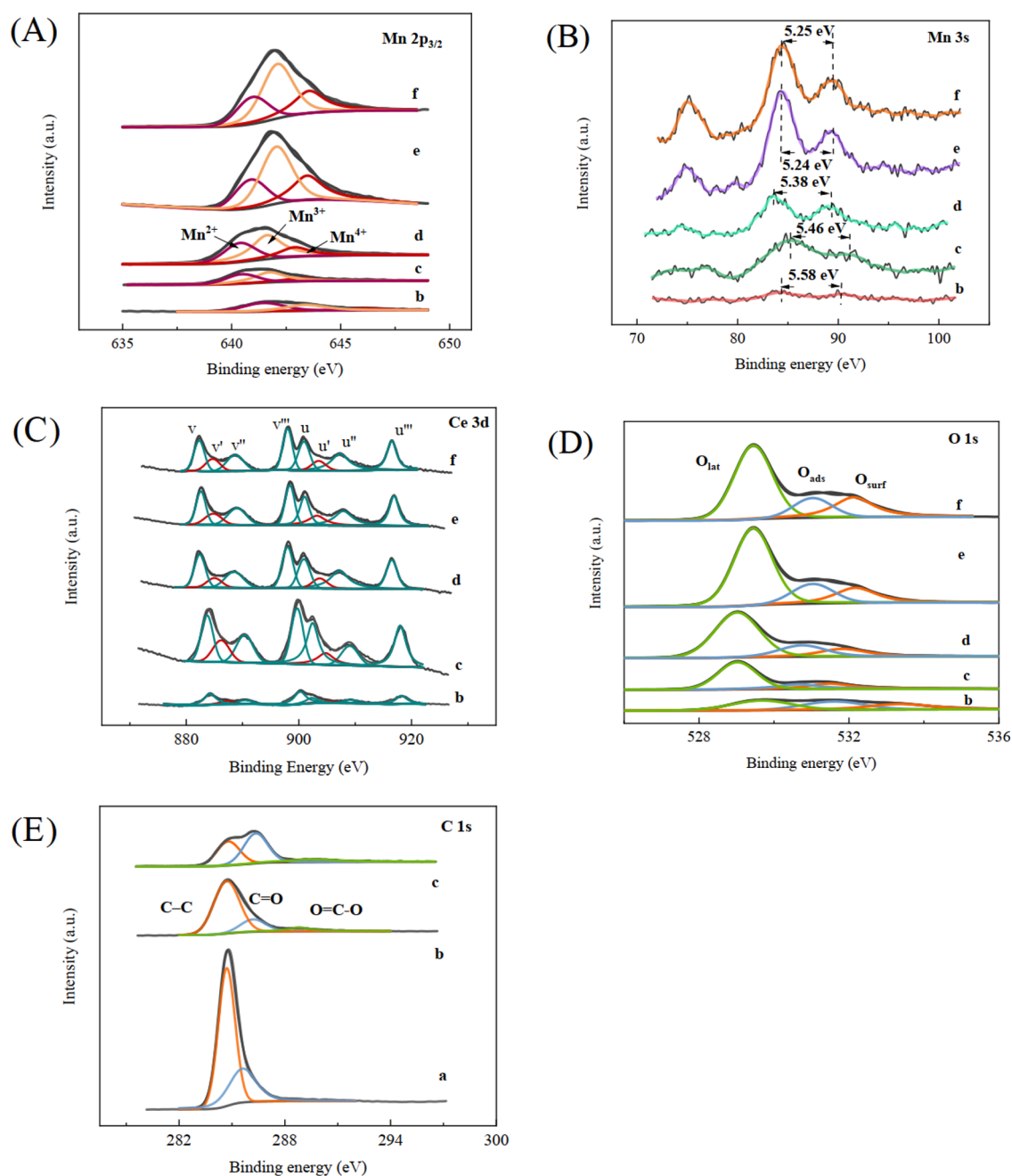
Figure 8. XPS spectra of (A) Mn $2p_{3/2}$, (B) Mn 3s, (C) Ce 3d, (D) O 1s, and (E) C 1s for (a) carbon nanospheres, (b) carbon@MnO_2/CeO_2, (c) MnO_2/CeO_2 hollow spheres, (d) used MnO_2/CeO_2 hollow spheres, (e) MnO_2/CeO_2, and (f) used MnO_2/CeO_2 samples.

Table 2. Summary of XPS Data of Fresh and Used Catalysts

	Mn $2p_{3/2}$			Mn 3s	O 1s			Ce 3d		
	Mn^{2+}/Mn	Mn^{3+}/Mn	Mn^{4+}/Mn	AOS	O_{lat}	O_{ads}	O_{surf}	Ce^{3+}	Ce^{4+}	atomic % (Mn/Ce)
carbon nanosphere					13.7%	26.4%	59.9%			
carbon@MnO_2/CeO_2	46.7%	39.7%	13.7%	2.40	38.3%	33.0%	28.7%	11.7%	88.3%	∼2:3
MnO_2/CeO_2 hollow spheres	34.6%	50.0%	15.5%	2.86	64.0%	17.0%	19.0%	14.2%	85.8%	∼5:7
used MnO_2/CeO_2 hollow spheres	29.9%	50.2%	19.9%	2.85	67.3%	18.6%	14.1%	14.3%	85.7%	
MnO_2/CeO_2	22.4%	50.0%	27.6%	3.06	66.0%	16.9%	17.1%	21.4%	78.6%	∼2:1
used MnO_2/CeO_2	21.9%	51.4%	26.7%	3.05	61.7%	15.7%	22.6%	24.5%	75.5%	

To understand the ingredient difference, an atomic % test by XPS was conducted in this work as shown in Tables 2 and 3. The ratio of Mn/Ce is close to 2:1 in MnO_2/CeO_2, while the ratio of Mn/Ce is much less than 2:1 for MnO_2/CeO_2 hollow spheres and carbon@MnO_2/CeO_2, which reveals the manganese oxide embedded inside the catalysts. Noteworthily, $KMnO_4$ in aqueous solution quickly reacted with the C sphere and then generated a carbon@MnO_2 structure. Thus, the

Table 3. Summary of the Element Content of Catalysts

	atomic %[a]		
	C	Mn	Ce
carbon@MnO$_2$/CeO$_2$	71.79	2.28	3.16
MnO$_2$/CeO$_2$ hollow spheres	26.05	6.11	8.99
MnO$_2$/CeO$_2$		10.19	5.47

[a]Obtained from XPS data.

unoxidized graphitic (C−C/C═C) chain breaks and bonds with manganese and oxygen to form short chains.[25] The surface of the carbon core decomposed to short chains simultaneously with outward diffusion. The inward diffused MnO$_4^−$ and faster outward diffused carbon chains formed a diffusion couple, which was supplemented for carbon@MnO$_2$ architecture generation. Also, parts of unreacted MnO$_2$ particles were deposited on the carbon sphere surface (the Kirkendall diffusion). Therefore, the Mn/Ce ratio on the MnO$_2$/CeO$_2$ hollow sphere surface is less than that on the surface of MnO$_2$/CeO$_2$.

In addition, we used O 1s XPS spectroscopy to characterize the active surface oxygen species directly (Figure 8D). Three types of surface oxygen species can be identified. The peaks located at ~529.5, ~531, and ~533 eV are ascribed to the lattice oxygen O$^{2−}$ (O$_{lat}$), surface-adsorbed species (O$_{ads}$), and adsorbed molecular water (O$_{surf}$), respectively. The molar ratios of O$_{surf}$, O$_{ads}$, and O$_{lat}$ are listed in Table 2. It is found that the O$_{ads}$ ratio of MnO$_2$/CeO$_2$ hollow spheres (17.0%) is higher than that of MnO$_2$/CeO$_2$ (16.9%). Also, for MnO$_2$/CeO$_2$ hollow spheres, the concentration of O$_{ads}$ increased to 18.6% after the continuity test. In the case of MnO$_2$/CeO$_2$, the concentration of O$_{ads}$ species decreased to 15.7% after the continuity test. The O$_{lat}$ of MnO$_2$/CeO$_2$ hollow spheres is richer (64% → 67%) after the continuity test (Table 2), while that for MnO$_2$/CeO$_2$ has decreased (66% → 62%). Also, lattice oxygen is the primary factor for the balance between Mn(IV)/Mn(III), Mn(II)/Mn(III), and Ce(III)/Ce(IV), which is important for the catalyst stability. Moreover, the O binding energy of MnO$_2$/CeO$_2$ hollow spheres is lower than that of MnO$_2$/CeO$_2$, which could be attributed to the

existence of oxygen vacancies, leading to the increased electron density of O.

The XPS spectra of carbon are also compared between different samples in Figure 8E. The peaks were deconvoluted into three major peaks corresponding to C−C (sp$_2$ carbon), C═O, and O═C−O at the binding energies of ~284.8, ~286.4, and ~289.2 eV, respectively.[26] It can be seen that the C−C peak decreases with the Mn/Ce coating, while the oxidized carbon (C═O and O═C−O groups) increases, indicating the broken C−C bond and the generation of C═O/O═C−O bands corresponding with the FTIR results. The performance and characterization analysis above indicate that the existence of C improves the structural stability and electronic conductivity of the MnO$_2$/CeO$_2$ hollow spheres.

Compared to carbon@MnO$_2$/CeO$_2$, a shift to the higher binding energy in MnO$_2$/CeO$_2$ hollow sphere C 1s is observed, as the number of bonds between O/Mn and C increases, in accordance with the shift of Mn 2p$_{3/2}$ and O 1s for MnO$_2$/CeO$_2$ hollow spheres. In addition, according to the results of TG−DTG and XPS, the bonded carbon contributes to the chemical stability and transfer of the electrons to Mn/O, which is attributed to the generation of oxygen vacancies and more active oxygen species. The above analyses prove that the combination of carbon and MnO$_2$/CeO$_2$ has an excellent synergistic catalytic effect via interfacial electron transfer.

In conclusion, due to the higher ratio of Mn(II) and Mn(III) for MnO$_2$/CeO$_2$ hollow spheres, which is related to the formation of oxygen vacancies to maintain charge balance and more active oxygen species, the HCHO removal performance of the MnO$_2$/CeO$_2$ hollow sphere catalyst was improved. As the XPS results prove, the higher ratio of Mn(II) and Mn(III) for MnO$_2$/CeO$_2$ hollow spheres is attributed to the electrons transferring from C and Ce. We believe that this is the important reason for the superior low-temperature (20−40 °C) catalytic performance of MnO$_2$/CeO$_2$ hollow spheres due to the use of carbon spheres as the sacrificial template.

3.6. Stability of Catalysts. Adaptability to the actual environment is a crucial aspect in HCHO degradation. Therefore, the high GHSV and stability tests were conducted. For changing the GHSV, in MnO$_2$/CeO$_2$ hollow spheres, the HCHO conversion is about 84% at GHSV = 60,000 mL (g$_{cat}$
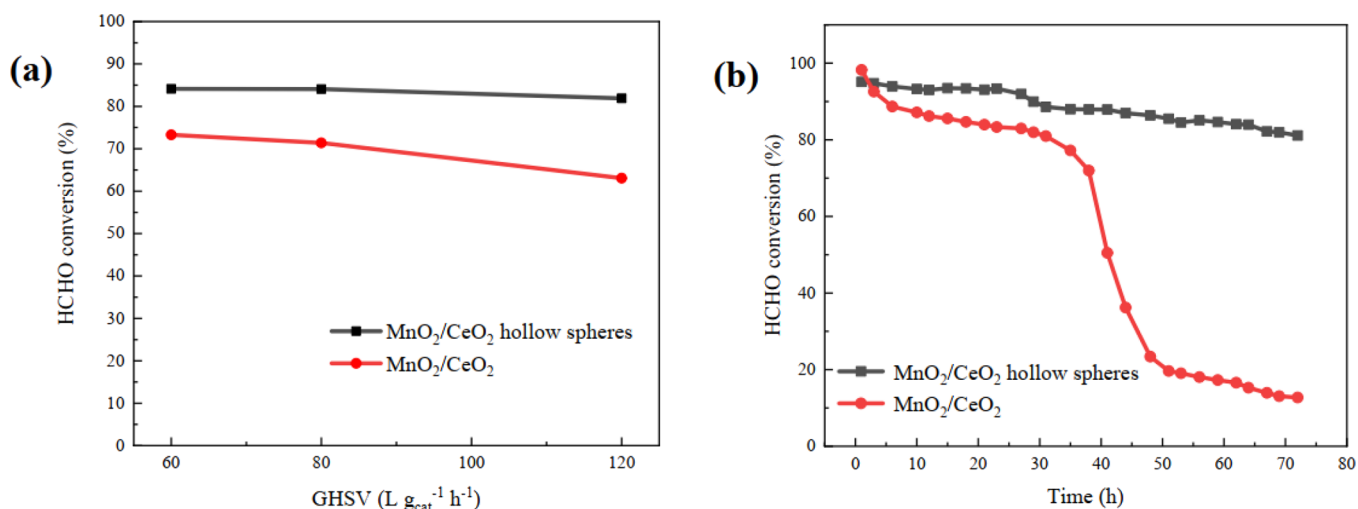

Figure 9. (a) GHSV effect (GHSV = 60, 80, and 120,000 mL (g$_{cat}$ h)$^{−1}$) and (b) stability test (50 °C) for HCHO removal (RH = 50%) over the MnO$_2$/CeO$_2$ hollow spheres and MnO$_2$/CeO$_2$ samples.

h)$^{-1}$ and decreases slightly to 82% at GHSV = 120,000 mL (g$_{cat}$ h)$^{-1}$, as shown in Figure 9a. Meanwhile, as for MnO$_2$/CeO$_2$, in the same circumstances, the HCHO conversion was about 73% at GHSV = 60,000 mL (g$_{cat}$ h)$^{-1}$, decreasing to 63% at GHSV = 120,000 mL (g$_{cat}$ h)$^{-1}$.

To assess the stability of the catalysts, we performed the continuity test at 50 °C with GHSV = 50,000 mL (g$_{cat}$ h)$^{-1}$. By comparing performances of the two catalysts (Figure 9b), it is found that the stability of MnO$_2$/CeO$_2$ hollow spheres is significantly higher than that of MnO$_2$/CeO$_2$. For MnO$_2$/CeO$_2$, the HCHO conversion decreases to 13% after 72 h. In contrast, the performance of MnO$_2$/CeO$_2$ hollow spheres is relatively stable for 72 h time on stream, and the conversion of HCHO is maintained at 81%. The performances of MnO$_2$/CeO$_2$ hollow spheres show its high efficiency for HCHO degradation and good stability.

3.7. Intermediates and Mechanism. To research into the specific reaction intermediates and route of formaldehyde oxidation, in situ DRIFTS measurement was conducted on MnO$_2$/CeO$_2$ hollow spheres under different atmospheres. First, it was exposed to 20 ppm of HCHO/N$_2$ flow for 120 min and then to a pure O$_2$ flow for another 60 min. When exposed to HCHO/N$_2$, the adsorbed HCHO ($\sim$1071 cm^{-1}), the dioxymethylene (DOM) species (1526 cm^{-1}), and δ(CH) ($\sim$1372 cm^{-1}) and vas(COO−) ($\sim$1600 cm^{-1}) of formate species can be observed in Figure 10. These results suggest that
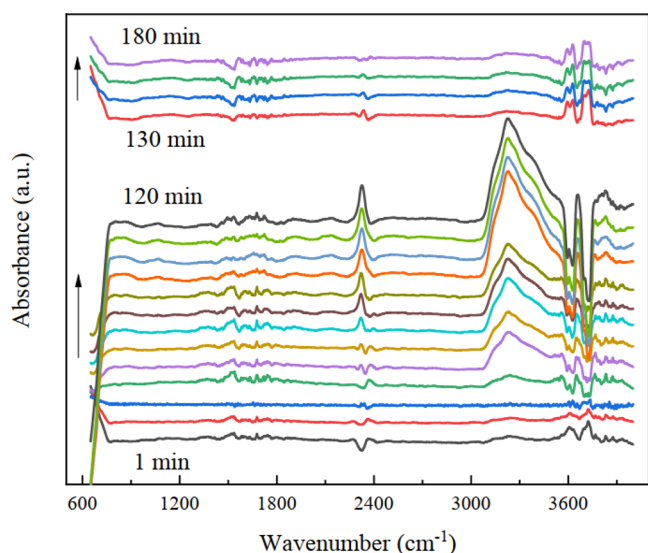
**Figure 10.** In situ DRIFTS spectra of the HCHO adsorption and HCHO removal of MnO$_2$/CeO$_2$ hollow spheres.

DOM and formate species are the dominating primary intermediate reaction products. As the reaction proceeded, the ν(CO) vibrations (1681 cm^{-1}) of carbonate species, adsorbed hydroxyl group (3260 cm^{-1}),[27] and adsorbed carbon dioxide (2327 cm^{-1}) were accumulated. However, the intensity of the OH group band ($\sim$3610 cm^{-1}) decreased.[28] According to the in situ infrared results, it can be seen that HCHO mainly adsorbed on active sites, which was converted into DOM species via OH groups, and oxidized into formate and carbonate species during the adsorption process. The adsorption of reactants is the first step for HCHO oxidation, which plays a key role for the oxidation reaction.

After 120 min, oxygen was injected into the reaction chamber. Under the flow of O$_2$, the band intensities for DOM, formate, and carbonate species, which immediately reacted with O$_2$, showed the opposite changing trend and almost disappeared. The intensity of OH groups ($\sim$3610 cm^{-1}) increases compared with that before the feeding of O$_2$, implying that H$_2$O was continuously generated on the MnO$_2$/CeO$_2$ hollow sphere surface. Finally, the intensity of the adsorbed carbon dioxide (2327 cm^{-1}) peak[29] becomes weaker, indicating that carbonate species were decomposed and released as gaseous CO$_2$ in this reaction.

A possible reaction route of formaldehyde removal on the MnO$_2$/CeO$_2$ hollow sphere catalyst is depicted in Figure 11
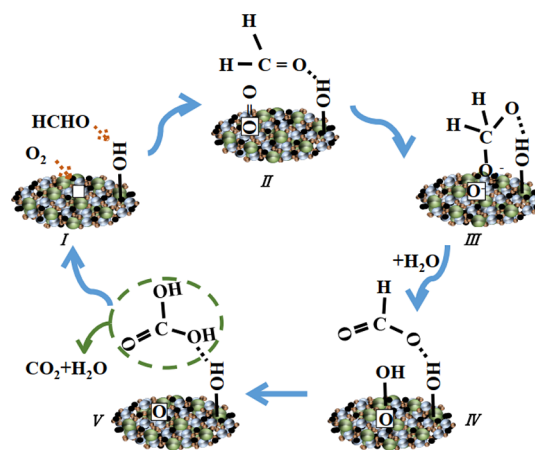
Figure 11. Proposed mechanism and pathways of HCHO removal with the MnO$_2$/CeO$_2$ hollow sphere catalyst.

based on in situ DRIFTS results. The HCHO molecule is first adsorbed on the MnO$_2$/CeO$_2$ hollow sphere surface via H-bonding with the OH groups (step 1). Step 2 shows the dissociation processes of oxygen on the catalyst surface; the O$_2$ activation is achieved. Subsequently, one active oxygen atom attacks the electrophilic carbon atom of the adsorbed formaldehyde molecule, leading to the generation of a DOM intermediate (step 3). After that, DOM transforms into more stable formate species through molecular rearrangement. Then, surface OH groups are generated on the MnO$_2$/CeO$_2$ hollow sphere surface via decomposition of H$_2$O and the active O atom from the O vacancies[30] (step 4). Finally, CO$_2$ and H$_2$O are produced through the reaction between formate species and surface OH groups, and the catalyst surface returns to its original state (step 5). According to this mechanistic view, through using the carbon sphere as a self-sacrificing template, the interaction between Mn/Ce and carbon increases the oxygen vacancies and adsorption sites, therefore synergistically enhancing the generation of active oxygen species, which is one of the key factors to the efficient HCHO removal.

4. CONCLUSIONS

This study focuses on the influence of using the carbon sphere as a self-sacrificing template on the catalytic performance and structural and chemical properties of MnO$_2$/CeO$_2$ hollow spheres. Due to carbon enhancing the electron transfer efficiency, the interaction between Mn/Ce and carbon increases. This increase in the interaction strength seems to (i) increase the oxygen vacancy, (ii) promote the oxygen species mobility, and (iii) improve the chemical stability of the

MnO_2/CeO_2 hollow spheres, resulting in the significantly improved performance of the MnO_2/CeO_2 hollow spheres compared to MnO_2/CeO_2. These entire properties are beneficial to the low-temperature, high GHSV oxidation performance and long-life stability of the MnO_2/CeO_2 hollow spheres in HCHO removal.

ASSOCIATED CONTENT

Supporting Information

The Supporting Information is available free of charge at https://pubs.acs.org/doi/10.1021/acsomega.1c04769.

> EDS mappings; Arrhenius plots for HCHO removal; FTIR spectra of the catalysts; N_2 adsorption−desorption isotherms and the corresponding pore size distribution curves; electron paramagnetic resonance (EPR) spectra of the catalysts (PDF)

AUTHOR INFORMATION

Corresponding Authors

Wenzhi Li − *Laboratory of Basic Research in Biomass Conversion and Utilization, Department of Thermal Science and Energy Engineering, University of Science and Technology of China, Hefei 230026, China;* orcid.org/0000-0002-7082-5839; Email: liwenzhi@ustc.edu.cn

Qi Zhang − *CAS Key Laboratory of Renewable Energy, Guangzhou Institute of Energy Conversion, Chinese Academy of Sciences, Guangzhou 510640, PR China;* orcid.org/0000-0003-4840-0129; Email: zhangqi@ms.giec.ac.cn

Authors

Chen Zhu − *Laboratory of Basic Research in Biomass Conversion and Utilization, Department of Thermal Science and Energy Engineering, University of Science and Technology of China, Hefei 230026, China*

Shengnan Guan − *Laboratory of Basic Research in Biomass Conversion and Utilization, Department of Thermal Science and Energy Engineering, University of Science and Technology of China, Hefei 230026, China;* orcid.org/0000-0003-3895-7695

Ajibola T. Ogunbiyi − *Laboratory of Basic Research in Biomass Conversion and Utilization, Department of Thermal Science and Energy Engineering, University of Science and Technology of China, Hefei 230026, China*

Kun Chen − *Laboratory of Basic Research in Biomass Conversion and Utilization, Department of Thermal Science and Energy Engineering, University of Science and Technology of China, Hefei 230026, China*

Complete contact information is available at:
https://pubs.acs.org/10.1021/acsomega.1c04769

Author Contributions

§C.Z. and S.G. contributed equally to this article.

Notes

The authors declare no competing financial interest.

ACKNOWLEDGMENTS

REFERENCES

(1) Chen, Y.; Liu, J.; Shang, J.; Zhu, T. Simulated reaction of formaldehyde and ambient atmospheric particulate matter using a chamber. *J. Environ. Sci. (China)* **2017**, *56*, 45−51.

(2) Li, L.; Li, L.; Wang, L.; Zhao, X.; Hua, Z.; Chen, Y.; Li, X.; Gu, X. Enhanced catalytic decomposition of formaldehyde in low temperature and dry environment over silicate-decorated titania supported sodium-stabilized platinum catalyst. *Appl. Catal., B* **2020**, *277*, 119216.

(3) Tang, W.; Li, X.; Zhong, Y.; Chen, X.; Liu, Y.; Ding, Z. Study on concentration levels and pollution characteristics of typical VOCs in indoor air of residential buildings in Shanghai. *Environ. Chem.* **2021**, *40*, 1038−1047.

(4) Guo, M.; Pei, X.; Mo, F.; Liu, J.; Shen, X. Formaldehyde concentration and its influencing factors in residential homes after decoration at Hangzhou, China. *J. Environ. Sci.* **2013**, *25*, 908−915.

(5) Tu, S.; Chen, Y.; Zhang, X.; Yao, J.; Wu, Y.; Wu, H.; Zhang, J.; Wang, J.; Mu, B.; Li, Z.; Xia, Q. Complete catalytic oxidation of formaldehyde at room temperature on MnxCo3-xO4 catalysts derived from metal-organic frameworks. *Applied Catalysis a-General* **2021**, *611*, 117975.

(6) Wang, C.; Li, Y.; Zheng, L.; Zhang, C.; Wang, Y.; Shan, W.; Liu, F.; He, H. A Nonoxide Catalyst System Study: Alkali Metal-Promoted Pt/AC Catalyst for Formaldehyde Oxidation at Ambient Temperature. *ACS Catal.* **2021**, *11*, 456−465.

(7) Chen, X.; Wang, H.; Chen, M.; Qin, X.; He, H.; Zhang, C. Co-function mechanism of multiple active sites over Ag/TiO2 for formaldehyde oxidation. *Appl. Catal., B* **2021**, *282*, 119543.

(8) Miao, L.; Wang, J.; Zhang, P. Review on manganese dioxide for catalytic oxidation of airborne formaldehyde. *Appl. Surf. Sci.* **2019**, *466*, 441−453.

(9) Yusuf, A.; Snape, C.; He, J.; Xu, H.; Liu, C.; Zhao, M.; Chen, G. Z.; Tang, B.; Wang, C.; Wang, J.; Behera, S. N. Advances on transition metal oxides catalysts for formaldehyde oxidation: A review. *Catalysis Reviews* **2017**, *59*, 189−233.

(10) Xu, H.; Yan, N.; Qu, Z.; Liu, W.; Mei, J.; Huang, W.; Zhao, S. Gaseous Heterogeneous Catalytic Reactions over Mn-Based Oxides for Environmental Applications: A Critical Review. *Environ. Sci. Technol.* **2017**, *51*, 8879−8892.

(11) Oh, W.-D.; Lua, S.-K.; Dong, Z.; Lim, T.-T. Performance of magnetic activated carbon composite as peroxymonosulfate activator and regenerable adsorbent via sulfate radical-mediated oxidation processes. *J. Hazard. Mater.* **2015**, *284*, 1−9.

(12) Zhang, L.; Xie, Y.; Jiang, Y.; Li, Y.; Wang, C.; Han, S.; Luan, H.; Meng, X.; Xiao, F. Mn-promoted Ag supported on pure siliceous Beta zeolite (Ag/Beta-Si) for catalytic combustion of formaldehyde. *Appl. Catal. B-Environ.* **2020**, *268*, 118461.

(13) Zhu, L.; Wang, J.; Rong, S.; Wang, H.; Zhang, P. Cerium modified birnessite-type MnO2 for gaseous formaldehyde oxidation at low temperature. *Appl. Catal., B* **2017**, *211*, 212−221.

(14) Ma, X.; Wen, J.; Guo, H.; Ren, G. Facile template fabrication of Fe-Mn mixed oxides with hollow microsphere structure for efficient and stable catalytic oxidation of 1,2-dichlorobenzene. *Chem. Eng. J.* **2020**, *382*, 122940.

(15) Meng, Q.; Cui, J.; Wang, K.; Tang, Y.; Zhao, K.; Huang, L. Facile preparation of hollow MnOx-CeO2 composites with low Ce content and their catalytic performance in NO oxidation. *Mol. Catal.* **2020**, *493*, 111107.

(16) Zeng, K.; Yu, H.; Sun, Z.; Yan, J.; Zheng, X.; Jiang, Y.; Hu, W.; Tian, J.; Yang, R. Enhanced Electrocatalytic Activity of Murdochite-Type Ni6MnO8 for Water Oxidation via Surface Reconstruction. *ACS Appl. Mater. Interfaces* **2020**, *12*, 39205−39214.

(17) Sun, X.; Li, Y. Colloidal carbon spheres and their core/shell structures with noble-metal nanoparticles. *Angew. Chem., Int. Ed.* **2004**, *43*, 597−601.

(18) Ou, C. C.; Chen, C. H.; Chan, T. S.; Chen, C. S.; Cheng, S. Influence of pretreatment on the catalytic performance of Ag/CeO2 for formaldehyde removal at low temperature. *J. Catal.* **2019**, *380*, 43−54.

(19) Zhang, Z.; Fan, Z.; Guo, H.; Fang, W.; Chen, M.; Shangguan, W. Effect of A(2+) and B3+ substitution for Cobalt on low-temperature catalytic removal of formaldehyde over spinel A(x)B(3-x)O(4) (A = Mg, Ni, Zn; B = Cr, Fe, Al). *Catal. Today* **2019**, *332*, 139−143.

(20) Zhang, J.; Jin, Y.; Li, C. Y.; Shen, Y. N.; Han, L.; Hu, Z. X.; Di, X. W.; Liu, Z. L. Creation of three-dimensionally ordered macroporous Au/CeO2 catalysts with controlled pore sizes and their enhanced catalytic performance for formaldehyde oxidation. *Appl. Catal. B-Environ.* **2009**, *91*, 11−20.

(21) Barai, H. R.; Rahman, M. M.; Rahim, A.; Joo, S. W. α-MnO2 nanorod/boron nitride nanoplatelet composites for high-performance nanoscale dielectric pseudocapacitor applications. *J. Ind. Eng. Chem.* **2019**, *79*, 115−123.

(22) Lykaki, M.; Pachatouridou, E.; Carabineiro, S. A. C.; Iliopoulou, E.; Andriopoulou, C.; Kallithrakas-Kontos, N.; Boghosian, S.; Konsolakis, M. Ceria nanoparticles shape effects on the structural defects and surface chemistry: Implications in CO oxidation by Cu/CeO2 catalysts. *Applied Catalysis B-Environmental* **2018**, *230*, 18−28.

(23) Andriopoulou, C.; Trimpalis, A.; Petallidou, K. C.; Sgoura, A.; Efstathiou, A. M.; Boghosian, S. Structural and Redox Properties of Ce1-xZrxO2-delta and Ce0.8Zr0.15RE0.05O2-delta (RE: La, Nd, Pr, Y) Solids Studied by High Temperature in Situ Raman Spectroscopy. *J. Phys. Chem. C* **2017**, *121*, 7931−7943.

(24) Ulyanov, A. N.; Maslakov, K. I.; Martin, C.; Yang, D. S.; Chernyak, S. A.; Markovich, V.; Savilov, S. V. Electronic structure of CaMn1-xNbxO3 (x=0.02, 0.04, 0.06 and 0.08) perovskites. Self-organization of terminal layers. *J. Alloys Compd.* **2020**, *820*.

(25) Zhao, Y.; Meng, Y.; Jiang, P. Carbon@MnO2 core-shell nanospheres for flexible high-performance supercapacitor electrode materials. *J. Power Sources* **2014**, *259*, 219−226.

(26) Patil, S.; Satilmis, B.; Uyar, T. Metal-free N-doped ultrafine carbon fibers from electrospun Polymers of Intrinsic Microporosity (PIM-1) based fibers for oxygen reduction reaction. *J. Power Sources* **2020**, *451*, 227799.

(27) Huang, K.; Kong, L.; Yuan, F.; Xie, C. In situ diffuse reflectance Fourier transform infrared spectroscopy (DRIFTS) study of formaldehyde adsorption and reactions on Pd-doped nano-gamma-Fe(2)O(3) films. *Appl. Spectrosc.* **2013**, *67*, 930−939.

(28) Du, X. Y.; Li, C. T.; Zhang, J.; Zhao, L. K.; Li, S. H.; Lyu, Y.; Zhang, Y. D.; Zhu, Y. C.; Huang, L. Highly efficient simultaneous removal of HCHO and elemental mercury over Mn-Co oxides promoted Zr-AC samples. *J. Hazard. Mater.* **2021**, *408*, 124830.

(29) Liu, F.; Liu, X.; Shen, J.; Bahi, A.; Zhang, S.; Wan, L.; Ko, F. The role of oxygen vacancies on Pt/NaInO2 catalyst in improving formaldehyde oxidation at ambient condition. *Chem. Eng. J.* **2020**, *395*, 125131.

(30) Chen, J.; Chen, W.; Huang, M.; Tang, H.; Zhang, J.; Wang, G.; Wang, R. Metal organic frameworks derived manganese dioxide catalyst with abundant chemisorbed oxygen and defects for the efficient removal of gaseous formaldehyde at room temperature. *Appl. Surf. Sci.* **2021**, *565*, 150445.